Acta Materialia 226 (2022) 117682

Contents lists available at ScienceDirect

Acta Materialia

journal homepage: www.elsevier.com/locate/actamat

Full length article

Inhomogeneous electric field-induced structural changes in soft lead zirconate titanate ferroelectric ceramics

Jianwei Zhao[a], Stephen D. Funni[b], Emily R. Molina[a], Elizabeth C. Dickey[b], Jacob L. Jones[a,*]

[a] Department of Materials Science and Engineering, North Carolina State University, Raleigh, NC 27695, United States
[b] Department of Materials Science and Engineering, Carnegie Mellon University, Pittsburgh, PA 15213, United States

ARTICLE INFO

Article history:
Received 22 November 2021
Revised 12 January 2022
Accepted 21 January 2022
Available online 22 January 2022

Keywords:
Lead zirconate titanate
X-ray diffraction
Ferroelectric
Domain switching
Phase transition

ABSTRACT

Under the application of an external voltage, high electric field concentrations can develop around the interdigitated electrode edges inside multilayer ceramic actuators (MLCAs). The spatial distribution of the local electrical field can create local inhomogeneity in the electromechanical response. To investigate the complex field inhomogeneity in MLCAs, partially electroded Nb-doped $PbZr_xTi_{1-x}O_3$ samples were investigated via synchrotron-based high-energy X-ray diffraction (XRD) as a function of applied electric field. These *in situ* experiments allowed us to probe the structural changes as a function of position relative to the electrode edge and calculate the local degree of domain alignment, from which the local electric field directions were inferred. The domain switching behavior, both in amplitude and orientation, was found to be spatially dependent across the inactive regions in partially electroded samples. Specifically, the degree of domain alignment and field-induced phase transitions are amplified near the electrode edge. The orientation-dependent phase transitions are also amplified for the tetragonal composition near the morphotropic phase boundary (MPB), i.e., the Nb-doped $PbZr_{0.53}Ti_{0.47}O_3$ composition. Finite element analysis (FEA) shows spatially-dependent, inhomogeneous electric field distributions in the partial-electrode samples, which closely match the experimentally inferred local electric field directions from XRD. The correlation of FEA and experimental data from XRD corroborates that the ferroelectric domain orientation distributions are being directed, primarily, in the direction of the electric field.

1. Introduction

Ferroelectric materials and devices have been developed and used in a wide variety of commercialized applications, including but not limited to various types of transducers, sensors, and actuators [1,2]. The dominant material for electromechanical applications is $PbZr_xTi_{1-x}O_3$ (PZT), because of its superior dielectric and piezoelectric properties [2–4]. Over past decades, PZT-based materials have been extensively studied to further enhance their piezoelectric performance [5–9]. It is worth noting that PZT-based ferroelectric materials exhibit improved properties, e.g., dielectric, piezoelectric, and electromechanical coupling coefficients, when the composition approaches the morphotropic phase boundary (MPB, x~0.52), where two phases coexist [10].

Under the application of an external voltage, a ferroelectric ceramic in a parallel plate capacitor geometry is often assumed to experience a homogeneous electric field. Such an assumption simplifies many experimental and computational models of ferroelectric devices. Nevertheless, inhomogeneous electric fields that differ in either field amplitude or direction may exist locally inside ferroelectric materials and devices. For example, under the application of an external voltage, inhomogeneous fields can develop inside a polycrystalline ferroelectric ceramic with chemical inhomogeneities or core-shell structures [11], distributed around a crack tip [12], or near the tip-sample interface in a piezoresponse force microscopy (PFM) measurement [13]. Inhomogeneous electric fields can also develop near the interdigitated electrode edges in complex-structured MLCAs [14–16]. Due to the electric field gradients near the interdigitated electrode edge, non-uniform strain will develop around the interdigitated electrode termination region, resulting in an inhomogeneous stress distribution inside an MLCA. Furthermore, local electric fields are highly inhomogeneous in the so-called “inactive regions” far away from the electrode terminations in multilayer devices, which experience a substantially lower electric field amplitude and, as a result, will not undergo as extensive electromechanical deformation in response to the externally applied voltage. However, there is a lack of deep understanding of how these electric field inhomogeneities affect local ferroelectric domain switching as well as field-induced phase transitions, which are especially likely to occur in materials with compositions near an MPB. Given that MLCAs are ubiquitous in ferroelectric actuators,

* Corresponding author.
E-mail address: jacobjones@ncsu.edu (J.L. Jones).

https://doi.org/10.1016/j.actamat.2022.117682
1359-6454/

e.g., for fuel-injectors due to their low driving voltage, high-strain generation, and quick response time, a more thorough understanding of the implications of electric field inhomogeneities on electromechanical behavior is needed.

A powerful approach which allows for measurement is synchrotron-based high-energy XRD, which has been broadly exploited to study the behavior of polycrystalline ferroelectrics *in situ* during application of electric fields. In particular, the penetrating power of the X-rays allows for interrogation of the bulk (vs. surface) of the specimens and the measurement of complete Debye-Scherrer diffraction rings in the transmitted direction. Using a two-dimensional (2D) area detector, *in situ* high-energy XRD with electric field application can reveal field-induced structural changes in ferroelectrics, e.g., changes in lattice distortions, domain switching, and phase transitions as a function of angle to the applied field direction and at different field amplitudes [17–18].

This paper utilizes the aforementioned approaches to characterize the inhomogeneous, electric field-induced domain switching behaviors and phase transitions in PZT-based ferroelectric ceramics with three different Nb-doped PZT compositions near the MPB with varying Zr:Ti ratios. The primary experimental tool is synchrotron-based *in situ* high-energy XRD using a micron-scale beam that is rastered through different spatial positions in the sample. By employing a monochromatic X-ray beam in a rastering mode, we derive unique micrometer-scale observations that characterize inhomogeneous effects in ferroelectrics, including but not limited to domain switching and phase transitions.

2. Materials and experiments

PZT pellets doped with 1% niobium of varied Zr:Ti ratios, including $PbZr_{0.50}Ti_{0.50}O_3$ (Nb-PZT 50/50), $PbZr_{0.53}Ti_{0.47}O_3$ (Nb-PZT 53/47), and $PbZr_{0.56}Ti_{0.44}O_3$ (Nb-PZT 56/44) were provided by PI Ceramic (PI Ceramic GmbH, Lederhose, Thuringia, Germany). The Nb^{5+} dopants substitute the Zr^{4+} or Ti^{4+} in the perovskite B-sites, resulting in the generation of A-site vacancies to form PZT materials into soft ferroelectrics [19,20]. Comparing to a hard ferroelectric ceramic, the soft ferroelectric ceramics promote domain switching and phase transitions more readily under the application of electric fields [19]. According to Ref. [21], the three Nb-PZT compositions exhibit a similar coercive field of approximately 1 kV/mm and a mean grain size of 6 μm. The crystal structures of both Nb-PZT 50/50 and Nb-PZT 53/47 are considered to be single-phase tetragonal (*P4mm*) in the virgin (as-processed, electrically unpoled) state, with the latter composition being closer to the MPB; the Nb-PZT 56/44 composition has a single rhombohedral phase (*R3m*) in the virgin state [21,22].

Fig. 1(a) shows a schematic of the experimental setup for the *in situ* high-energy XRD with the application of high-voltage to the specimen. Such an experimental setup has been commonly used to study domain switching and phase transitions in ferroelectrics as a function of applied electric fields in multiple prior works, though probing ferroelectric samples experiencing homogeneous electric field [22–28]. The X-ray beam energy was 105.7 keV (λ = 0.1173 Å), which penetrated the ceramic bars in transmission geometry. Rectangular ceramic bars of dimensions approximately 5 × 1 × 1 mm were cut from monolithic Nb-PZT pellets and painted with silver paste on two opposite parallel 5 × 1 mm surfaces to form electrodes, with a 1:2 ratio of the top and bottom electrodes. The ceramic bar was placed on a customized sample stage for the application of electric fields via a high-voltage amplifier (AMS-10B2, Matsusada Precision, Shiga-ken, Japan) that was driven by a wave function generator (Agilent 33220A, Keysight Technologies, Santa Rosa, CA). A unipolar electric field was applied to the samples, starting from 0 kV/mm in the virgin state to a maximum of 3 kV/mm and back to 0 kV/mm (remnant state), in steps

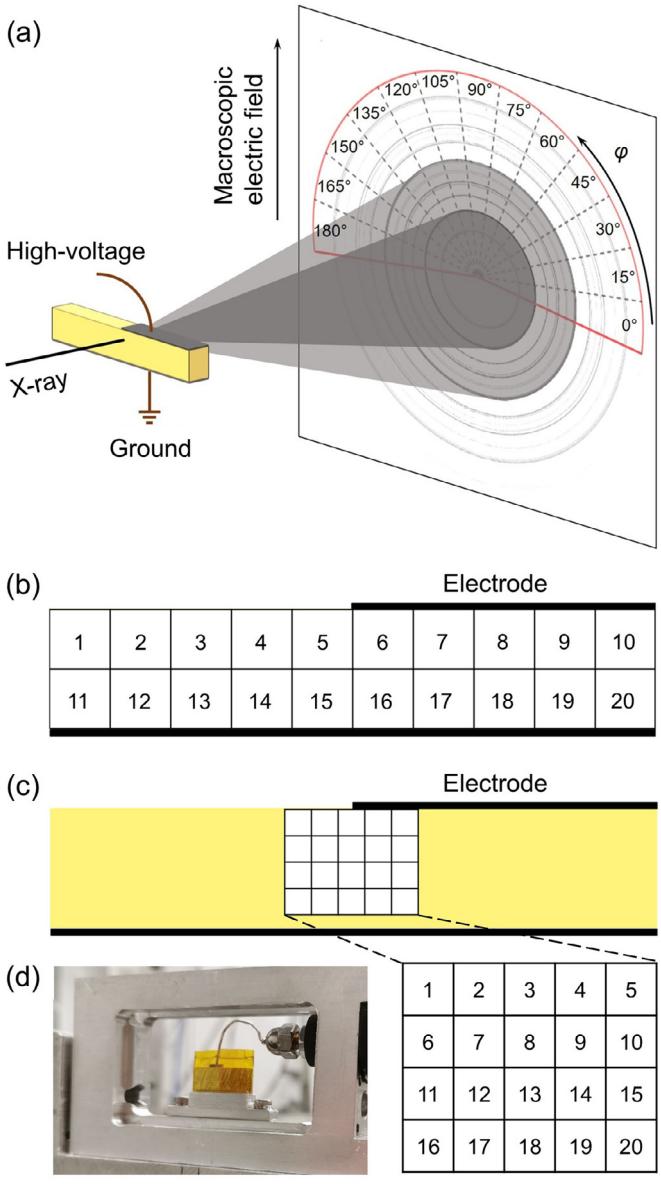

Fig. 1. Schematics of (a) the experimental setup at beamline 11-ID-C, APS, showing the partial-electrode sample with the (b) whole-bar-scan pattern in which each pixel is either 500 × 500 μm or 500 × 450 μm, (c) electrode-edge-scan pattern in which each pixel is 200 × 200 μm, and (d) customized sample stage.

of 1 kV/mm. The Debye-Scherrer diffraction rings, captured as 2D XRD patterns, were measured using an area detector that was located approximately 1500 mm away from the sample stage.

For each Nb-PZT composition, partial-electrode samples were measured twice, once each using two different scan patterns. Under the application of an external voltage, the partial-electrode sample is expected to have a homogeneous electric field (uniform local field directions and amplitudes) in the active region, which is the portion between the top and bottom electrodes; and an inhomogeneous electric field (non-uniform local field directions and amplitudes) in the inactive region, which is the portion uncovered with the top electrode. At each macroscopic electric field value, the X-ray beam scanned the partial-electrode sample following the sequence labeled in Fig. 1(b) and (c), which illustrate the experiments referenced as whole-bar-scan and electrode-edge-scan, respectively. In the whole-bar-scan experiment, depending on if a sample was slightly greater or less than 1 mm in height, a beam size (horizontal × vertical) of either 500 × 500 μm or

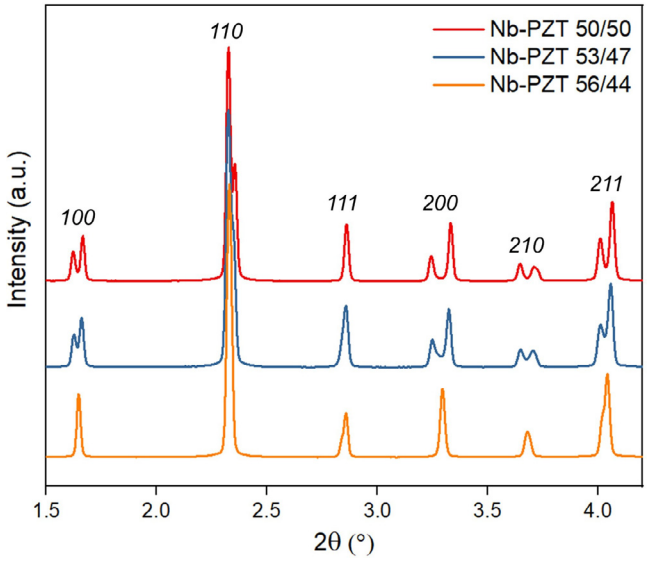

Fig. 2. XRD patterns for Nb-PZT 50/50, Nb-PZT 53/47, and Nb-PZT 56/44 at the virgin state with diffraction profiles relative to the pseudo-cubic perovskite phase.

500 × 450 μm was used, the latter of which helped to mitigate X-ray scattering from the silver electrodes in samples of 1 mm or thinner dimensions. For the electrode-edge-scan measurements, a smaller X-ray beam in size of 200 × 200 μm was employed to investigate the structural changes in response to field concentrations in the electrode termination region. In the 2D XRD patterns, the radial direction relates to the 2θ angle and the azimuthal angle (φ) represents an angle relative to the macroscopic field direction. As illustrated in Fig. 1(a), the top half of the 2D XRD pattern is divided into 13 sectors along the azimuthal direction, where each sector has an integration width of 15°. Each sector is integrated within the same 2θ range to generate equivalent one-dimensional (1D) XRD patterns through the open-access software, Fit2D [29]. Line Profile Analysis Software (LIPRAS) is used in the data analysis to fit multiple 1D XRD patterns efficiently and robustly at all azimuthal angles and field amplitudes [30].

3. Results and discussions

3.1. Crystallographic structure

In the virgin state, as shown in Fig. 2, the XRD plots reveal that all three sample types are single phase with Nb-PZT 50/50, Nb-PZT 53/47, and Nb-PZT 56/44 exhibiting tetragonal, tetragonal, and rhombohedral phases, respectively, which is consistent with that reported in Ref. [21,22]. The tetragonality (c/a) of Nb-PZT 50/50 is 1.027, whereas the near-MPB composition Nb-PZT 53/47 has a smaller c/a ratio of 1.023, resulting in a slightly narrower 2θ range between the 200 and 002 reflections. As the Zr/Ti ratio increases to 56/44, the 200 and 002 reflections merge, consistent with a single rhombohedral phase, along with the splitting of 111 peak into 111 and $11\bar{1}$ reflections.

3.2. Whole-bar-scan experiment

3.2.1. Structural changes under homogeneous electric fields

In the whole-bar-scan experiment, as shown in Fig. 1(b), pixels 6–10 and pixels 16–20 locate between the top and bottom electrodes, which is called the active region and is expected to experience a nearly homogeneous electric field. Using pixel 17 in the active region as an example, Fig. 3 presents the XRD patterns near the 002 and 200 reflections as a function of electric field for all three Nb-PZT compositions. The 002 and 200 reflections in the tetragonal phase (referred to as 002_T and 200_T) or the 111 and $11\bar{1}$ reflections in the rhombohedral phase (referred to as 111_R and $11\bar{1}_R$) are used to probe domain switching and phase transitions. In the virgin state, as shown in Fig. 3(a), (c), and (e), all reflections are nearly constant as a function of the azimuthal angle (φ) in all three Nb-PZT compositions, whereas the diffraction peaks change during the electric field application.

Fig. 3(b) shows the 002_T and 200_T reflections in the tetragonal phase Nb-PZT 50/50 under a macroscopic electric field of 3 kV/mm. Specifically, the intensities are shown to interchange (intensity from 002_T moves to 200_T or vice versa,) as a function of azimuthal angle (φ), which is a signature of electric field-induced ferroelectric/ferroelastic domain switching behaviors in a tetragonal phase ferroelectric material [31]. Similar intensity interchanges are also observed between 002_T and 200_T reflections in the tetragonal phase Nb-PZT 53/47, as shown in Fig. 3(d). Moreover, an additional peak also appears between the 002_T and 200_T reflections at approximately the 45° and 135° azimuthal angles in Nb-PZT 53/47 which indicates the emergence of a new phase under the application of electric field. The Nb-PZT 53/47 sample having a composition close to the MPB, where tetragonal and rhombohedral phases coexist. The emerged peak is consistent with the 200 reflection in the rhombohedral phase, therefore we have labelled it 200_R. The emergence of this reflection is only seen at specific azimuthal angles and the reason for this orientation-dependent field-induced phase transition from tetragonal ($P4mm$) to rhombohedral ($R3m$) was recently explained in Ref. [28]. In brief, Ref. [28] shows that only crystals with certain orientations relative to the electric field change phases, e.g., a tetragonal phase crystal in which the 111 pole is approximately parallel to the macroscopic field direction. In single crystals, these orientations are sometimes called "domain engineered" because they do not exhibit domain switching with electric field application.

Fig. 3(f) shows the diffraction pattern changes near the 111_R and $11\bar{1}_R$ reflections for the rhombohedral phase Nb-PZT 56/44 under a 3 kV/mm electric field. The 111_R is most intense in the direction parallel to the macroscopic field direction ($\varphi = 90°$). The 002_T and 111_R Bragg reflections correspond to (002) and (111) crystallographic planes in the tetragonal and rhombohedral perovskite phases, respectively. In these respective phases, the plane normals are parallel to [002] and [111] crystallographic directions, which are the polarization axes. Under the application of electric fields, the intensity change of 002_T and 111_R reflections correspond to the domain volume variations of 002-type and 111-type ferroelectric/ferroelastic domains. Parallel to the electric field direction, domain volumes of the 002-type and 111-type ferroelectric/ferroelastic domain increase, which results in intensified reflections. In contrast, the 002_T and 111_R reflections are weakest in sectors parallel to the 0° and 180° azimuthal angles, which indicates the volumes of 002-type and 111-type ferroelectric/ferroelastic domain orientations are decreased in directions perpendicular to the macroscopic field direction. This is consistent with the local electric field direction in this area of the sample being equivalent to the macroscopic field direction, as expected far from the electrode termination region.

We can further quantify the field-induced ferroelectric/ferroelastic domain texture using Eqs. (1) and (2), for tetragonal and rhombohedral phase ferroelectric ceramics, respectively [32].

$$f_{002(MRD)} = 3\,\frac{\frac{I_{002}}{I'_{002}}}{\frac{I_{002}}{I'_{002}} + 2\frac{I_{200}}{I'_{200}}} \tag{1}$$

$$f_{111(MRD)} = 4\,\frac{\frac{I_{111}}{I'_{111}}}{\frac{I_{111}}{I'_{111}} + 3\frac{I_{11\bar{1}}}{I'_{11\bar{1}}}} \tag{2}$$

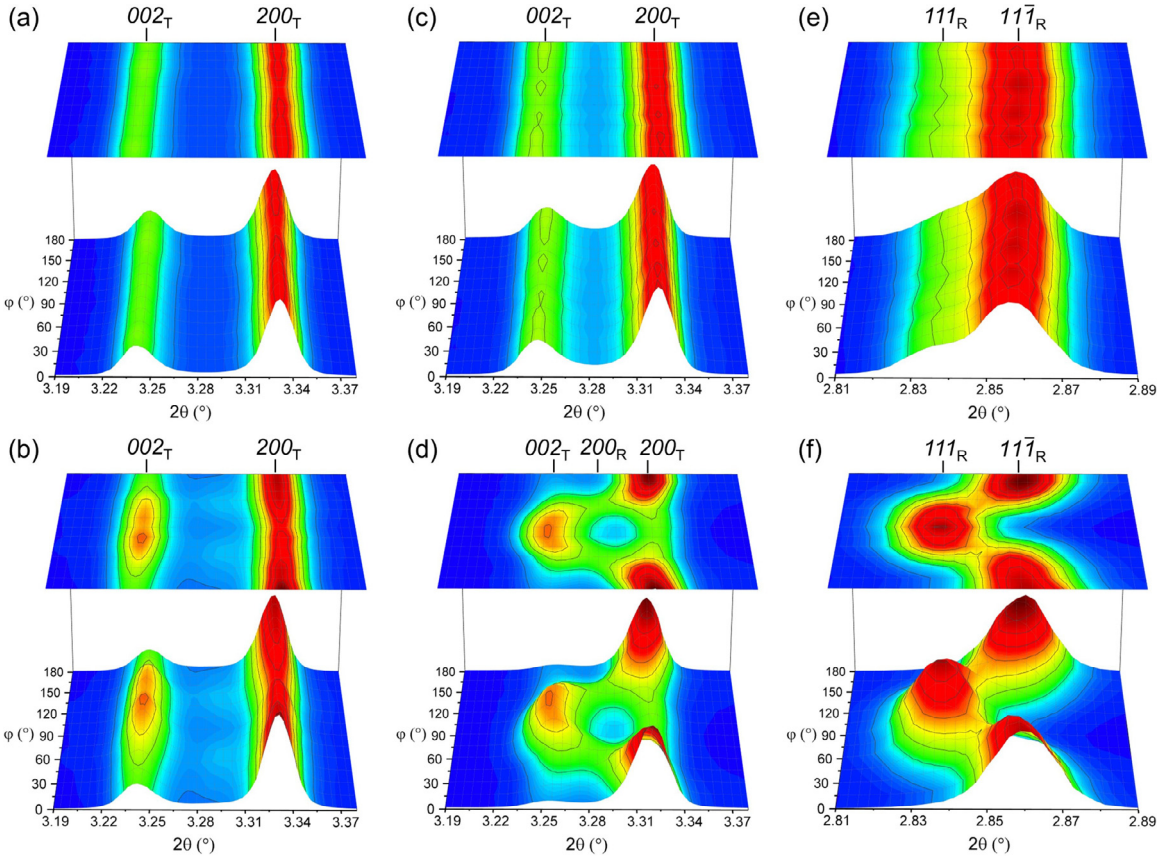

Fig. 3. In the active region, peak intensity as a function of azimuthal angle (φ) at the virgin state (top) and a homogeneous electric field of 3 kV/mm (bottom) for Nb-PZT 50/50 in (a) and (b), Nb-PZT 53/47 in (c) and (d), Nb-PZT 56/44 in (e) and (f). All data come from pixel 17 (Fig. 1(b)) in the active and field-homogeneous region in different compositions of Nb-PZT partial-electrode samples.

where I represents the integrated peak intensity at a given electric field, I' stands for the integrated peak intensity in the virgin state of a randomly-oriented polycrystalline sample. Multiple of a random distribution (MRD) is the unit used to describe pole densities or domain textures and f = 1.0 MRD would indicate that the domain volume fractions in that direction of the sample are equivalent to that of a virgin state. Values of $f_{002} = 3.0$ MRD and $f_{111} = 4.0$ MRD are the maximum theoretical values in tetragonal and rhombohedral phase perovskite ferroelectrics, which represents a saturated domain texture state in a given direction.

The integrated intensity of specific reflections is determined by profile fitting in LIPRAS [30] of the 1D XRD patterns in specific 2θ windows, at all azimuthal angles and all electric fields, simultaneously. The analysis process starts with a background fitting of the 1D XRD patterns using 2θ windows of approximately 3.0–3.55° for 002_T and 2.7–3.0° for 111_R. Using pixel 17 in the active region as a representative example, Fig. 4 shows the calculated f_{002} under the macroscopic 3 kV/mm for Nb-PZT 50/50 and Nb-PZT 53/47, and f_{111} for Nb-PZT 56/44, as a function of azimuthal angle (φ). All three Nb-PZT compositions show the strongest domain preference parallel to the 90° azimuthal angle. In particular, Nb-PZT 50/50 experiences a maximum of $f_{002} = 1.52$ MRD, whereas Nb-PZT 53/47 experiences a maximum of $f_{002} = 2.15$ MRD, indicating that more extensive domain switching occurs in the tetragonal composition that is in closer proximity to the MPB. Using the tetragonal Nb-PZT 50/50 composition as an example, prior to application of electric fields, the f_{002} value is ~1.0 at all azimuthal angles. Under the application of an electric field, the 002 poles are more preferred in directions more closely aligned with the field direction (φ from 60°~120°) because [002] is the polarization direction in a tetragonal perovskite; in contrast, in directions more perpendicular to the electric field direction (φ<30° or φ>150°), the relative fraction of 002 poles decreases which results in f_{002} values less than 1.0. Similar trends can be found in f_{002} of Nb-PZT 53/47 and f_{111} of PZT 56/44. In addition, the maximum 111 degree of domain

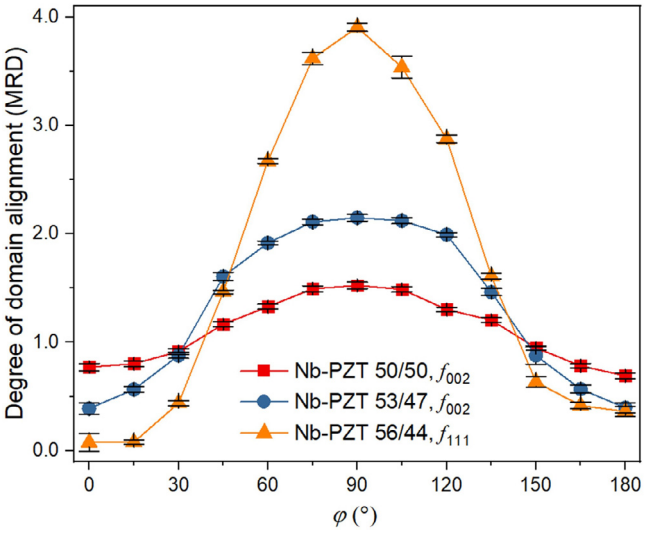

Fig. 4. At the macroscopic 3 kV/mm, degree of domain alignment of Nb-PZT 50/50, Nb-PZT 53/47, and Nb-PZT 56/44 as a function of azimuthal angle (φ). All data come from pixel 17 (Fig. 1(b)) in the active and field-homogeneous region in different compositions of Nb-PZT partial-electrode samples.

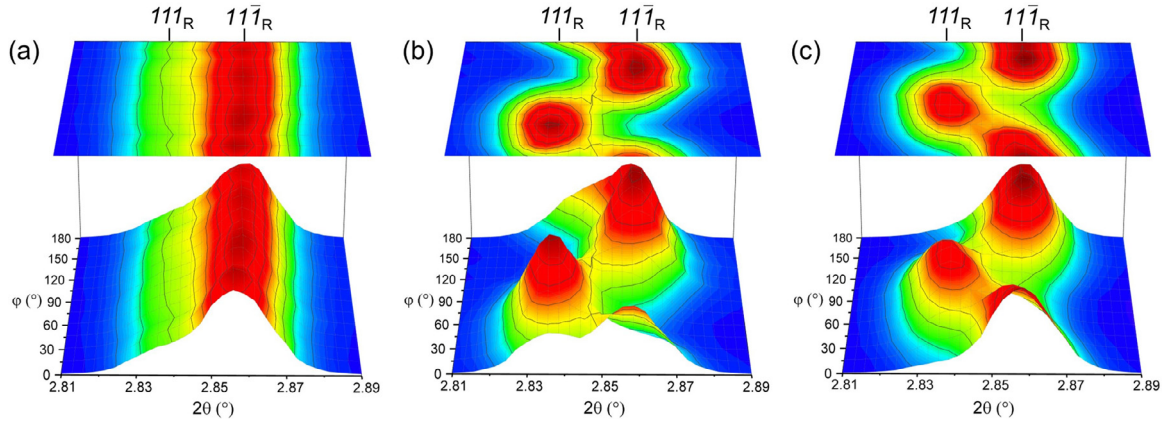

Fig. 5. At the macroscopic 3 kV/mm, 111 peak intensity changes as a function of azimuthal angle (φ) for (a) pixel 1, (b) pixel 5, and (c) pixel 14 from the inactive region of Nb-PZT 56/44 partial-electrode sample in the whole-bar-scan experiment.

alignment in the rhombohedral phase Nb-PZT 56/44 composition is $f_{111} = 3.90$ MRD, which is much higher than the f_{002} achieved in the tetragonal compositions and very nearly the theoretical maximum. This observation is consistent with prior work and is attributed to the rhombohedral phase having, relative to the tetragonal phase, a smaller spontaneous ferroelastic strain (which reduces intergranular stresses) and more domain variant options [22,32].

3.2.2. Structural changes under inhomogeneous electric field

In the region where there is no top electrode, pixels 1–5 and pixels 11–15 in Fig. 1(b), the material is expected to experience an inhomogeneous electric field in both amplitude and direction. We would expect the local ferroelectric/ferroelastic domain texture to be a function of the electric field amplitude and direction, with the maximum degree of domain alignment expected parallel to the direction of the local electric field. By determining the directionality of domain alignment locally, the local electric field direction in each scanned pixel can therefore be inferred. Diffraction peaks as a function of azimuthal angle and under the macroscopic 3 kV/mm are shown in Fig. 5 for three representative pixels from the rhombohedral phase Nb-PZT 56/44 partial-electrode sample measured at a resolution of 500 × 500 μm. Pixel 1 is located in the so-called inactive region that is far from the top electrode edge, where the sample is expected to experience a negligible local electric field. As presented in Fig. 5(a), the intensity ratios between the 111_R and $11\bar{1}_R$ reflections at the macroscopic 3 kV/mm do not change as a function of azimuthal angle, indicating that the sample remains isotropic in its local domain texture. Therefore, we consider pixel 1 to be experiencing a negligible electric field amplitude. Fig. 5(b) presents peak intensity changes from pixel 5 in the inactive region that is immediately next to the top electrode edge. Compared to pixel 1, pixel 5 shows domain texture, i.e., changes in relative intensities as a function of azimuthal angle. Specifically, the strongest 111_R reflection intensity and, thus, 111 domain preference is at an azimuthal angle near 45°, which suggests the local electric field direction in pixel 5 is parallel to the 45° angle, i.e., tilting towards the top electrode edge. Additionally, a 111 domain preference is also found in pixel 14, as shown in Fig. 5(c), and the strongest intensity of the 111_R peak is not at 90°, which means the local electric field direction is not parallel to the macroscopic field direction.

Though the local field direction may be inferred by the azimuthal angle that exhibits the highest intensity of the 111_R reflection, a more robust and convincing methodology involves calculating the domain textures, i.e., degree of domain alignment according to Eq. (2) as a function of azimuthal angle, for all scanned pixels and using these results to quantitatively determine the local

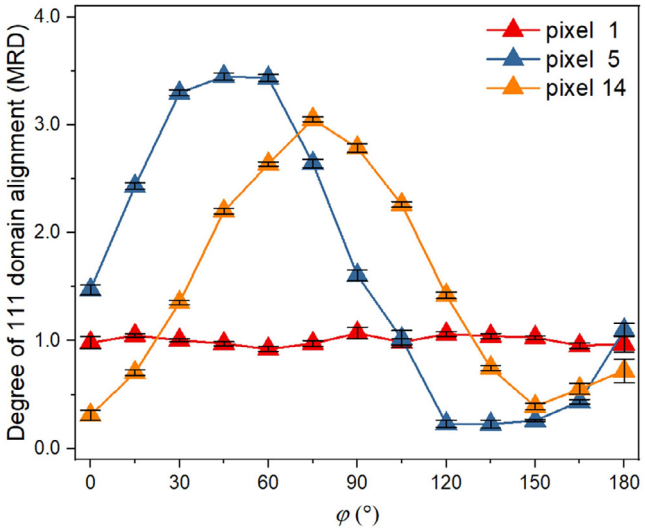

Fig. 6. At the macroscopic 3 kV/mm, degree of 111 domain alignment as a function of azimuthal angle (φ) for pixel 1, pixel 5, and pixel 14 from the inactive region of Nb-PZT 56/44 partial-electrode sample with the whole-bar-scan pattern.

electric field directions. Fig. 6 shows the f_{111} for the three representative pixels in the rhombohedral phase Nb-PZT 56/44 partial-electrode sample at of the macroscopic 3 kV/mm. The data show negligible errors for the most azimuthal angles. The calculated f_{111} for pixel 1 is approximately a value of 1.0 at all azimuthal angles, with a maximum $f_{111} = 1.07$ MRD along the 90° orientation, consistent with the absence of a local electric field. However, moving towards the electrode edge, pixel 5 exhibits a maximum $f_{111} = 3.45$ MRD parallel to the 45° azimuthal angle. Pixel 14, which is located further from the electrode edge in the inactive region, has a maximum $f_{111} = 3.05$ MRD value parallel along the 75° azimuthal angle. Compared to pixel 5, pixel 14 experiences a weaker local electric field amplitude and in a distinguishably different direction. These orientation-dependent domain switching behaviors from representative pixels are consistent with the observations in the raw data, i.e., the contour plots shown in Fig. 5. Similar analyses are performed for all scanned pixels in the tetragonal composition Nb-PZT partial-electrode samples and the raw data, i.e., contour plots, and the quantification of 002 domain preference in representative pixels are provided in Fig. S1–S4 in the Supplementary Information.

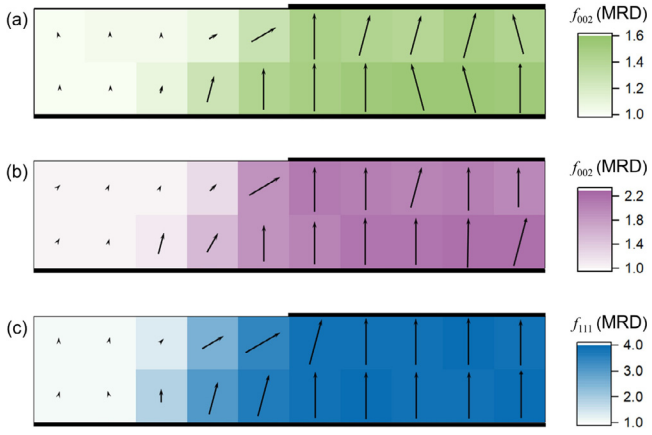

Fig. 7. At the macroscopic 3 kV/mm, the maximum degree of domain alignment and inferred local electric field vectors in each scanned pixel from the (a) Nb-PZT 50/50, (b) Nb-PZT 53/47, and (c) Nb-PZT 56/44 whole-bar-scan experiments.

The above analyses provide evidence that local electric field directions in individual pixels can be inferred by the maximum degree of domain alignment, i.e., f_{002} in tetragonal and f_{111} in rhombohedral ferroelectrics. Integrating all of these results for all pixels and compositions, Fig. 7 presents the experimentally-inferred local field direction. The color represents the maximum degree of domain alignment in each scanned pixel. The darker the color, the stronger the domain alignment. The arrow directions represent the local electric field vector inferred from domain alignments. Specifically, the direction of an arrow shows the azimuthal angle that exhibits the maximum degree of domain alignment and the arrow lengths correlate with the pole density values shown in the legend. For all compositions shown in Fig. 7, the spatial distribution of domain alignment (as represented by the color changes) are comparable, suggesting that the inhomogeneous electric fields are similar regardless of the specific composition nor the crystallographic phase. Specifically, in the active region underneath the top electrode, the degree of domain alignment is not significantly spatially dependent due to the homogeneous electric fields experienced in this region. However, in the inactive region, the degree of domain alignment decreases with increasing distance from the electrode edge because the local electric field amplitudes are weaker. The directions of the arrows also change in the inactive region, revealing the spatially dependent local electric fields in this region. Tables S1–S3 in the Supplementary Information tabulate the maximum degree of domain alignment and inferred local electric field directions in all scanned pixels from the whole-bar-scan experiments.

3.2.3. Finite element analysis (FEA)

To complement the synchrotron-based *in situ* high-energy XRD experiments, we performed FEA of the partial-electrode sample configuration to predict the electric field states throughout the sample at a 3 kV/mm macroscopic field. A 2D model was created, incorporating static electrical and mechanical physics to fully account for the effects of piezoelectric response. The model was meshed with 20 μm square elements overall. To accurately capture the discontinuity occurring at the top electrode edge, the model was meshed with increasingly smaller elements in the surrounding region, down to 0.5 μm in the immediate electrode edge region. Full tensor permittivity and piezoelectric properties were used for an undoped, poled PZT ceramic with a composition near the MPB [33]. Since the partial electrode geometry creates a locally varying poling direction, the properties were locally aligned for each element in the FEA model by the following process: first the electric field distribution was simulated using anisotropic permittivity; next each element in the model was assigned the anisotropic properties with the polarization axis aligned to the previously calculated field direction. With this model definition, the full electromechanical simulation was solved to estimate the electric field distribution in the sample during the experiment.

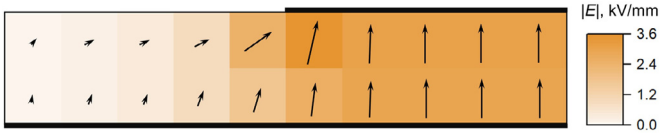

Fig. 8. Simulated local, average electric field amplitude and direction, calculated using nodal information from the FEA, for each pixel measured in the XRD experiment. The arrow length and pixel color are corresponding to the amplitude range from 0.07 to 3.55 kV/mm.

The macroscopic electric field is set at 3 kV/mm in the simulation, and the FEA solution yields an average 2D electric field vector calculated for each model element. To find the average electric field predicted for each pixel region in the experimental sample, an average of the elemental field vectors in the corresponding model region was taken on a component-wise basis, weighting by the size of the elements. In Fig. 8, the modeled average fields are shown mapped to the XRD scan pattern. The simulated, average field amplitude for the 500 μm pixels in the whole-bar-scan varies from 0.07 to 3.55 kV/mm. Detail of the simulated, averaged local field amplitude and direction are provided in Table S4 in the Supplementary Information. The simulated highest field 3.55 kV/mm in pixel 6 suggests that field concentration exists near the electrode edge. Similar to the experimental results, the FEA demonstrates the more homogeneous electric fields in the active region: average field directions and magnitudes converge to the applied field.

To integrate the experimental and simulation results, Fig. 9(a) shows the maximum degree of domain alignment as a function of simulated electric field amplitudes for pixels in the whole-bar-scan experiments. Fig. 9(a) only shows data from pixels with simulated electric field values above the coercive field (1.0 kV/mm), or pixels exhibiting high degree of domain alignment (>1.1 MRD, regarded as showing measurable domain switching). By selectively evaluating data from pixels above the coercive field, we are able to exclude data near the ferroelectric coercive field, where large nonlinearities are expected to occur. Fig. 9(a) shows that, for tetragonal phase Nb-PZT compositions, the experimentally-determined f_{002} exhibits close linear correlation with the simulated field amplitudes for data from pixels above the coercive field. In the rhombohedral phase Nb-PZT 56/44, the calculated f_{111} also exhibits close linear correlation with the simulated field amplitude at field amplitudes above the coercive field. Fig. 9(b) plots the experimentally inferred local electric field direction as a function of the simulated field direction for probed pixels in Nb-PZT partial-electrode samples. The dashed line represents the case in which the simulated field direction is equivalent to the experimentally-inferred field direction. Fig. 9(b) demonstrates that the simulated electric field directions from FEA correlate well with the field directions inferred from the *in situ* high-energy XRD experiments. Given the correlations between experiment and simulation, the simulated electric field amplitudes and directions in FEA could be used to predict the extent of domain switching and the preferred direction of domain alignment.

3.3. Electrode-edge-scan experiment

Given that there is an electric field concentration around the top electrode edge, higher resolution electrode-edge-scan experiments were also performed, as illustrated in Fig. 1(c). Using the

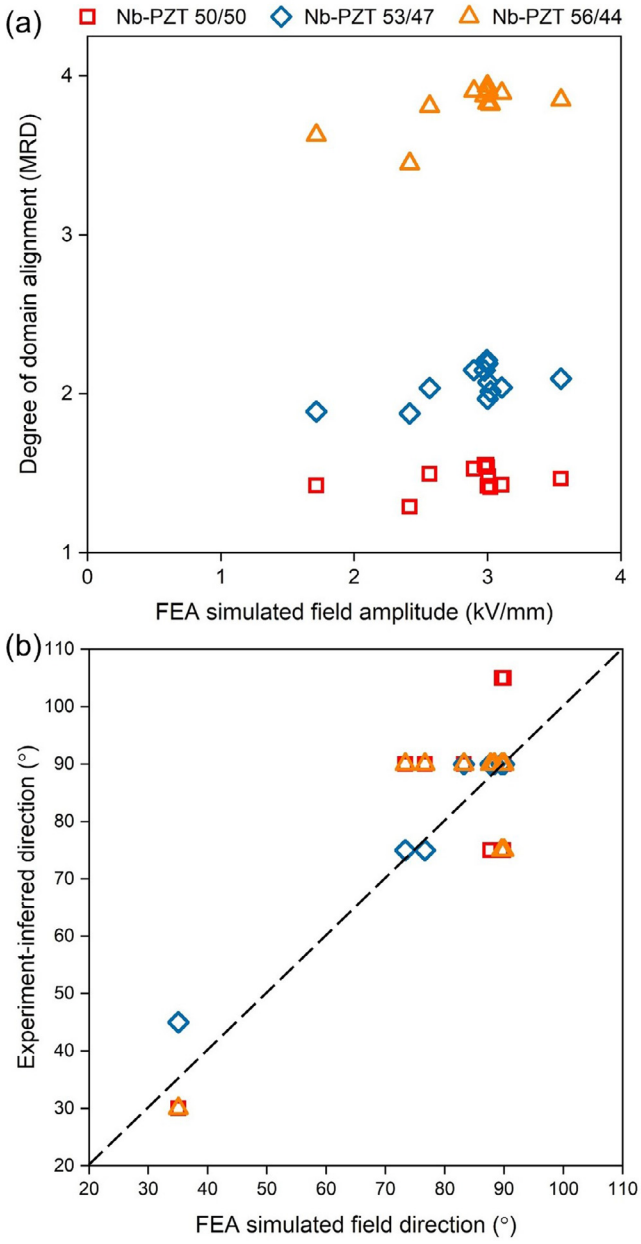

Fig. 9. (a) Correlation between the degree of domain alignment and simulated electric field amplitudes, and (b) correlation between the experimentally-inferred local electric field directions and simulated electric field directions from FEA of the whole-bar-scan experiment. Note: Only pixels with simulated electric field values above the coercive field (1.0 kV/mm), or pixels exhibiting high degree of domain alignment (>1.1 MRD, regarded as showing measurable domain switching) are used in correlations.

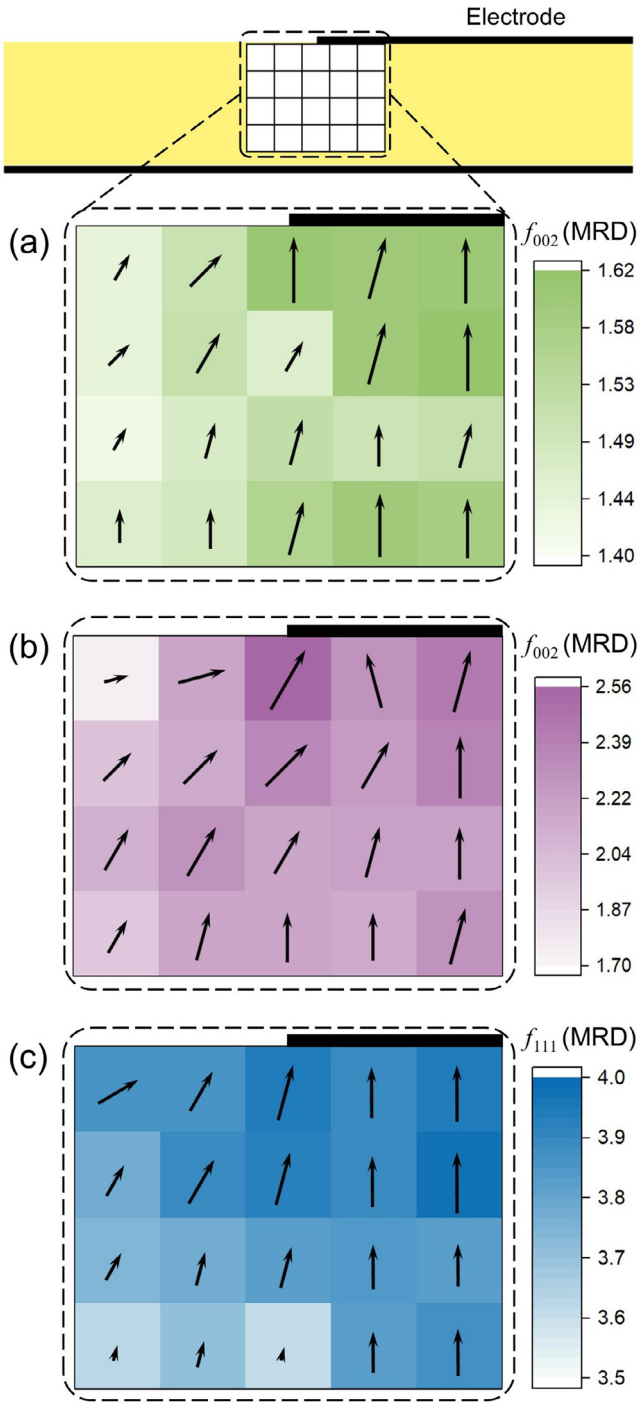

Fig. 10. At the macroscopic 3 kV/mm, the calculated maximum degree of domain alignment and inferred local electric field vectors in each scanned pixel from the (a) Nb-PZT 50/50, (b) Nb-PZT 53/47, and (c) Nb-PZT 56/44 electrode-edge-scan experiments.

approaches and calculations presented for the whole-bar-scan experiments, the local electric field direction in each scanned pixel of the electrode-edge-scan is inferred by calculating the maximum f_{002} or f_{111} for the tetragonal or rhombohedral phases, respectively. The results are illustrated in Fig. 10(a)–(c). As seen from color changes and local field vectors, all three compositions show obvious spatially dependent domain alignments in the electrode edge region. Besides the *in situ* high-energy XRD experiments, FEA was also performed for the electrode-edge-scan experiment. Detailed results are illustrated in Fig. S5 and tabulated in Table S8 in the Supplementary Information. At a macroscopic field of 3 kV/mm, the FEA shows that the local electric fields are highly variable around the electrode edge. As shown in Fig. S6, for all Nb-PZT compositions, the calculated maximum degree of domain alignment nearly has a linear correlation with the simulated local electric field. Furthermore, the experiment-inferred field directions and the simulated field directions near the electrode edge also correlate well.

Table 1 summarizes the maximum degree of domain alignment achieved in Nb-PZT partial-electrode samples with the whole-bar-scan and electrode-edge-scan patterns. As shown in Table 1, for Nb-PZT 50/50 electrode-edge-scan experiment at the macroscopic 3 kV/mm, the calculated maximum f_{002}= 1.61 MRD, which

Table 1
Under the macroscopic 3 kV/mm, the calculated maximum degree of domain alignment in Nb-PZT partial-electrode samples.

Nb-PZT	Crystallographic phase	Degree of domain alignment	Whole-bar-scan (MRD)	Electrode-edge-scan (MRD)
50/50	*P4mm*	$f_{002,\ max}$	1.55	1.61
53/47	*P4mm*, near MPB	$f_{002,\ max}$	2.21	2.55
56/44	*R3m*	$f_{111,\ max}$	3.94	3.97

is higher than the maximum f_{002}= 1.55 MRD observed in the same composition whole-bar-scan experiment. The comparison reveals an increased domain alignment near the electrode edge, indicative of a local electric field concentration. Similar observations are found in Nb-PZT 53/47 partial-electrode sample, showing the maximum f_{002}= 2.55 MRD, which is higher than what is observed in the same composition whole-bar-scan experiment, i.e., maximum f_{002}= 2.21 MRD. As for Nb-PZT 56/44 partial-electrode sample, the maximum f_{111} = 3.97 MRD and 3.94 MRD are calculated for the electrode-edge-scan and whole-bar-scan experiments, which are extremely close to the theoretical saturation value, i.e., f_{111} = 4.0 MRD in a rhombohedral phase ferroelectric. As aforementioned, since there are more domain variant options (i.e., polarization states) and smaller spontaneous ferroelastic strain (correlating with smaller 2θ range between 111_R and $11\bar{1}_R$ reflections), domain switching is expected to be more significant in Nb-PZT 56/44. Based on the correlation in Fig. 9(b), Nb-PZT 56/44 achieves a high $f_{111}$when the local field magnitudes are greater than 2 kV/mm. This saturation phenomenon explains why the two obtained maximum f_{111} are quite similar in the partial-electrode experiments with different scan patterns.

It is emphasized that, near the electrode edge in Nb-PZT 53/47, not only is domain alignment enhanced, but also the orientation-dependent tetragonal-to-rhombohedral phase transitions are amplified. Fig. 11 shows a comparison of peak intensity changes in two representative pixels, pixel 3 and pixel 19, from the electrode termination region in the Nb-PZT 53/47 partial-electrode sample. The contour plots in Fig. 11(a) and (b) show both strong domain alignment and orientation-dependent phase transitions, as evidenced by peak intensity interchanges as a function of angle and the appearance of 100_R between the 001_T and 100_T reflections in selective angles. In the electrode-edge-scan experiment, the X-ray beam scattered from the top electrode, resulting in a weak silver peak, 200_C ($Fm\bar{3}m$) that emerged at 2θ = 3.29°. The peak is between 002_T and 200_T, approximately $3.22° < 2\theta < 3.35°$, as shown in Fig. S7 in the Supplementary Information. Because XRD of silver does not generate a Bragg peak around the 001_T and 100_T reflections, they are intentionally used in Fig. 11. As concluded from Fig. 10(b), the experimentally inferred local electric field directions are parallel to 60° and 90° azimuthal angles in pixel 3 and pixel 19, respectively. Since the tetragonal-to-rhombohedral phase transitions occur 45° from field direction in the Nb-PZT 53/47 compo-

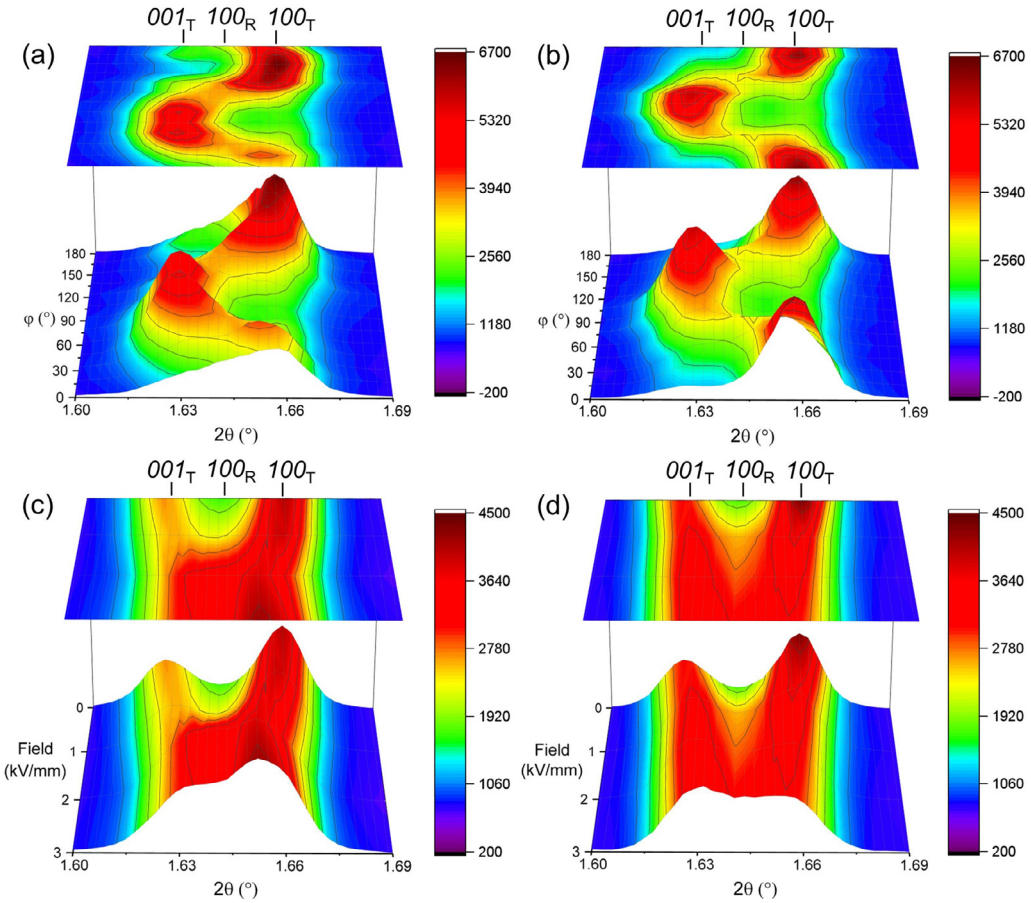

Fig. 11. The 100 profile intensity changes in representative pixels from Nb-PZT 53/47 electrode-edge-scan experiment. Plots (a) and (b) show the peak intensities as a function of the azimuthal angle (φ) at the macroscopic 3 kV/mm for pixel 3 and 19, respectively; Plots (c) and (d) show the peak intensities in response to macroscopic field amplitude in the azimuthal sector 45° away from the local field direction for pixel 3 and 19, respectively.

sition, the amplification of phase transition can be more obviously evidenced by comparing the field-dependent evolution of 100_R reflection in the azimuthal sector along the 15° and 45° azimuthal angle, as exhibited in Fig. 11(c) and (d), where these angles are 45° from the local field directions in corresponding pixels. At the macroscopic 3 kV/mm, the 100_R reflection in the 15° azimuthal angle in pixel 3 (Fig. 11(c)) is stronger than that in the 45° azimuthal angle in pixel 19 (Fig. 11(d)), indicating that the local electric field amplitude near the electrode edge is significantly amplified.

4. Conclusions

This work presents the local-scale domain switching and phase changes due to electric field inhomogeneity near electrode edges using a synchrotron-based experimental approach complemented by FEA. Specifically, under the application of macroscopic electric fields, the domain switching in a partial-electrode sample exhibits strong orientation-dependence and position-dependence, which is evidenced by the calculated degree of domain alignment and inferred local electric field directions. Near the electrode edge in partial-electrode samples, there exists strong local field concentrations, which can enhance the domain switching behaviors and amplify the field-induced phase transitions. In particular, for the Nb-PZT 53/47, which is compositionally next to the MPB, the tetragonal-to-rhombohedral phase transitions along selective azimuthal angles, corresponding to the local electric field vectors, are amplified near the electrode edge. FEA simulations of the local electric field show a good correlation with the experimentally inferred local field directions. This work demonstrates a useful approach for probing orientation-sensitive and spatially dependent structural changes in ferroelectric ceramics and devices. The observations from partial-electrode samples offer new insight to help understand inhomogeneous, field-induced structural changes in ferroelectric ceramics and devices. The significant domain switching and amplified phase transitions near the electrode edges, in particular, can be used in modeling and designing next-generation multilayered devices with high relevance to materials in close proximity to phase transitions.

Declaration of Competing Interest

The authors declare that they have no known competing financial interests or personal relationships that could have appeared to influence the work reported in this paper.

Acknowledgments

This material is based upon work supported by the National Science Foundation (NSF), as part of the Center for Dielectrics and Piezoelectrics (CDP) under Grant Nos. IIP-1841453 and IIP-1841466. The authors appreciate PI Ceramic for providing ferroelectric materials for study. This work was performed in part at the Analytical Instrumentation Facility (AIF) at North Carolina State University, which is supported by the State of North Carolina and the National Science Foundation (award number ECCS-2025064). The AIF is a member of the North Carolina Research Triangle Nanotechnology Network (RTNN), a site in the National Nanotechnology Coordinated Infrastructure (NNCI). This research used resources of the Advanced Photon Source, a U.S. Department of Energy (DOE) Office of Science User Facility operated for the DOE Office of Science by Argonne National Laboratory under Contract No. DE-AC02-06CH11357.

Supplementary materials

Supplementary material associated with this article can be found, in the online version, at doi:10.1016/j.actamat.2022.117682.

References

[1] P. Muralt, Ferroelectric thin films for micro-sensors and actuators: a review, J. Micromechanics Microengineering 10 (2) (2000) 136–146 Jun., doi:10.1088/0960-1317/10/2/307.
[2] L.E. Cross, Ferroelectric materials for electromechanical transducer applications, Mater. Chem. Phys. 43 (2) (1996) 108–115, doi:10.1016/0254-0584(95)01617-4.
[3] P. Muralt, A. Member, PZT thin films for microsensors and actuators-where do we stand, IEEE Transactions on Ultrasonics, Ferroelectrics, and Frequency Control 47 (4) (2000) 903–915, doi:10.1109/58.852073.
[4] S. Gebhardt, L. Seffner, F. Schlenkrich, A. Schönecker, PZT thick films for sensor and actuator applications, J. Eur. Ceram. Soc. 27 (13–15) (2007) 4177–4180, doi:10.1016/j.jeurceramsoc.2007.02.122.
[5] J.F. Ihlefeld, D.T. Harris, R. Keech, J.L. Jones, J.P. Maria, S. Trolier-Mckinstry, Scaling effects in perovskite ferroelectrics: fundamental limits and process-structure-property relations, Journal of the American Ceramic Society 2557 (2016) 6–9, doi:10.1111/jace.14387.
[6] X. Du, J. Zheng, U. Belegundu, K. Uchino, Crystal orientation dependence of piezoelectric properties of lead zirconate titanate near the morphotropic phase boundary, Appl. Phys. Lett. 72 (19) (1998) 2421–2423, doi:10.1063/1.121373.
[7] D.V. Taylor, D. Damjanovic, Piezoelectric properties of rhombohedral Pb(Zr, Ti)O_3 thin films with (100), (111), and 'random' crystallographic orientation, Appl. Phys. Lett. 76 (12) (2000) 1615–1617, doi:10.1063/1.126113.
[8] Y. Tan, et al., Unfolding grain size effects in barium titanate ferroelectric ceramics, Sci. Rep. 5 (2015) 9953, doi:10.1038/srep09953.
[9] Q.M. Zhang, H. Wang, N. Kim, L.E. Cross, Direct evaluation of domain-wall and intrinsic contributions to the dielectric and piezoelectric response and their temperature dependence on lead zirconate-titanate ceramics, J. Appl. Phys. 75 (1) (1994) 454–459, doi:10.1063/1.355874.
[10] D. Damjanovic, Ferroelectric, dielectric and piezoelectric properties of ferroelectric thin films and ceramics, Rep. Prog. Phys. 61 (9) (2002) 1267–1324, doi:10.1088/0034-4885/61/9/002.
[11] G. Wang, et al., Ultrahigh energy storage density lead-free multilayers by controlled electrical homogeneity, Energy Environ. Sci. 12 (2) (2019) 582–588, doi:10.1039/c8ee03287d.
[12] J.L. Jones, et al., Crack tip process zone domain switching in a soft lead zirconate titanate ceramic, Acta Mater. 55 (16) (2007) 5538–5548, doi:10.1016/j.actamat.2007.06.012.
[13] A. Gruverman, A. Kholkin, Nanoscale ferroelectrics: processing, characterization and future trends, Rep. Prog. Phys. 69 (8) (2006) 2443–2474, doi:10.1088/0034-4885/69/8/R04.
[14] T. Zhu, F. Fang, W. Yang, Fatigue crack growth in ferroelectric ceramics below the coercive field, J. Mater. Sci. Lett. 18 (13) (1999) 1025–1027, doi:10.1023/A:1006663108103.
[15] H. Cao, A.G. Evans, Electric-field-induced fatigue crack growth in piezoelectrics, J. Am. Ceram. Soc. 77 (7) (1994) 1783–1786, doi:10.1111/j.1151-2916.1994.tb07051.x.
[16] W. Qiu, Y.L. Kang, Q.H. Qin, Q.C. Sun, F.Y. Xu, Study for multilayer piezoelectric composite structure as displacement actuator by Moiré interferometry and infrared thermography experiments, Mater. Sci. Eng. A 452-453 (2007) 228–234, doi:10.1016/j.msea.2006.10.165.
[17] J.E. Daniels, A. Pramanick, J.L. Jones, Time-resolved characterization of ferroelectrics using high-energy X-ray diffraction, IEEE Trans. Ultrason. Ferroelectr. Freq. Control 56 (8) (2009) 1539–1545.
[18] A. Pramanick, J.E. Daniels, J.L. Jones, Subcoercive cyclic electrical loading of lead zirconate titanate ceramics II: time-resolved X-ray diffraction, J. Am. Ceram. Soc. 92 (10) (2009) 2300–2310, doi:10.1111/j.1551-2916.2009.03219.x.
[19] D. Viehland, Effect of uniaxial stress upon the electromechanical properties of various piezoelectric ceramics and single crystals, J. Am. Ceram. Soc. 89 (3) (2006) 775–785, doi:10.1111/j.1551-2916.2005.00879.x.
[20] R. Gerson, Variation in ferroelectric characteristics of lead zirconate titanate ceramics due to minor chemical modifications, J. Appl. Phys. 31 (1) (Jan. 1960) 188–194, doi:10.1063/1.1735397.
[21] "Computergestützte multiskalenmodellierung zur virtuellen entwicklung polykristalliner ferroelektrischer materialien (COMFEM). Report," 2010.
[22] C. Zhao, et al., Deconvolved intrinsic and extrinsic contributions to electrostrain in high performance, Nb-doped Pb(Zr_xTi_{1-x})O_3piezoceramics ($0.50 \leq x \leq 0.56$), Acta Mater. 158 (2018) 369–380, doi:10.1016/j.actamat.2018.08.006.
[23] G. Tutuncu, L. Fan, J. Chen, X. Xing, J.L. Jones, Extensive domain wall motion and deaging resistance in morphotropic $0.55Bi(Ni_{1/2}Ti_{1/2})O_3$-$0.45PbTiO_3$ polycrystalline ferroelectrics, Appl. Phys. Lett. 104 (13) (2014) 1–5, doi:10.1063/1.4870506.
[24] D.A. Ochoa, et al., Extensive domain wall contribution to strain in a (K,Na)NbO_3-based lead-free piezoceramics quantified from high energy X-ray diffraction, J. Eur. Ceram. Soc. 36 (10) (2016) 2489–2494, doi:10.1016/j.jeurceramsoc.2016.03.022.
[25] J.E. Daniels, W. Jo, J. Rödel, V. Honkimäki, J.L. Jones, Electric-field-induced phase-change behavior in $(Bi_{0.5}Na_{0.5})TiO_3$-$BaTiO_3$- $(K_{0.5}Na_{0.5})NbO_3$: a combinatorial investigation, Acta Mater. 58 (6) (2010) 2103–2111, doi:10.1016/j.actamat.2009.11.052.
[26] J.E. Daniels, W. Jo, J. Roedel, J.L. Jones, Electric-field-induced phase transformation at a lead-free morphotropic phase boundary. Case study in a 93%$(Bi_{0.5}Na_{0.5})TiO_3$-7%$BaTiO_3$ piezoelectric ceramic, Appl. Phys. Lett. 95 (3)

(2009) 032904/1–032904/3 F. Full J. TitleApplied Phys. Lett., doi:10.1063/1.3182679.

[27] M.C. Ehmke, N.H. Khansur, J.E. Daniels, J.E. Blendell, K.J. Bowman, Resolving structural contributions to the electric-field-induced strain in lead-free (1 - xBa($Zr_{0.2}Ti_{0.8}$)O_{3-x}($Ba_{0.7}Ca_{0.3}$)TiO_3 piezoceramics, Acta Mater. 66 (2014) 340–348, doi:10.1016/j.actamat.2013.11.021.

[28] J. Zhao, S.D. Funni, E.R. Molina, E.C. Dickey, J.L. Jones, Orientation-dependent, field-induced phase transitions in soft lead zirconate titanate piezoceramics, J. Eur. Ceram. Soc. 41 (6) (2021) 3357–3362, doi:10.1016/j.jeurceramsoc.2021.01.043.

[29] A.P. Hammersley, S.O. Svensson, M. Hanfland, A.N. Fitch, D. Hausermann, Two-dimensional detector software: from real detector to idealised image or two-theta scan, High Press. Res. 14 (4–6) (1996) 235–248, doi:10.1080/08957959608201408.

[30] G. Esteves, K. Ramos, C. Fancher, and J. Jones, "LIPRAS: line-profile analysis software." 2017, doi:10.13140/RG.2.2.29970.25282/3.

[31] J.L. Jones, E.B. Slamovich, K.J. Bowman, Domain texture distributions in tetragonal lead zirconate titanate by X-ray and neutron diffraction, J. Appl. Phys. 97 (3) (2005) 1–6, doi:10.1063/1.1849821.

[32] A. Pramanick, D. Damjanovic, J.E. Daniels, J.C. Nino, J.L. Jones, Origins of electro-mechanical coupling in polycrystalline ferroelectrics during subcoercive electrical loading, J. Am. Ceram. Soc. 94 (2) (2011) 293–309, doi:10.1111/j.1551-2916.2010.04240.x.

[33] D. Berlincourt, H.H. a. Krueger, and C. Near, "Properties of morgan electro ceramic ceramics," Techanical Publ. TP-226, Morgan Electro Ceram., pp. 1–12, 2000, Accessed: Jul. 30, 2020. [Online]. Available: www.morgan-electroceramics.com.